University of Crete - Department of Materials Science and Technology

Foundation for Research & Technology Hellas – Institute of Electronic Structure and Laser (FORTH/IESL)

Master thesis

Laser sintering of metal and semiconductor nanoparticles.

Student: Antonia Loufardaki

Supervisor: Associate Professor I. Remediakis

Co-supervisor: Doctor E. Stratakis

Heraklion, Crete, November 2020

Πανεπιστήμιο Κρήτης – Τμήμα Επιστήμης και Τεχνολογίας Υλικών

Ίδρυμα Τεχνολογίας και Έρευνας – Ινστιτούτο Ηλεκτρονικής Δομής και Λέιζερ (ΙΤΕ/ΙΗΔΛ)

Μεταπτυχιακή εργασία

Πυροσυσσωμάτωση Νανοσωματιδίων Μετάλλων και Ημιαγωγών με χρήση Ακτινοβολίας Λέιζερ.

Φοιτήτρια: Αντωνία Λουφαρδάκη

Επιβλέπων: Αναπληρωτής Καθηγητής Ιωάννης Ρεμεδιάκης

Συνεπιβλέπων: Δρ. Εμμανουήλ Στρατάκης

Ηράκλειο Κρήτης, Νοέμβριος 2020

Ευχαριστίες

"Γιατί όποιος δίχως πιβουλιά του πόθου του ξετρέχει,

εις μιάν αρχή α' βασανιστεί, καλό το τέλος έχει."

Ερωτόκριτος , Βιτσέντζος Κορνάρος
17^{ος} αιώνας

Table of contents

Abstract

Development of cost effective manufacturing methods will enable the production of large-scale flexible electronics such as solar panels or sensors. Laser processing has shown to be a promising candidate that offers a fast and non-destructive way to produce highly conductive patterns on flexible substrates.

The present study focuses on the investigation of the experimental parameters of laser sintering of printed Silver (Ag) lines on flexible substrates and Zinc Oxide (ZnO) structures on glass, using a Continuous Wave 455nm laser. Samples of different flexible substrates (kapton and FR4) and of different dimensions were irradiated using various irradiances, scanning speeds and two different scanning paths. Scanning Electron Microscopy (SEM) was applied for the morphological characterization of the samples, while electrical conductivity measurements were performed using a simple resistance measurement method.

Conclusions of the present work will be used to discuss the potentiality of the method in flexible electronic devices such as photovoltaics and gas sensors.

1. General overview:

1.1 Flexible electronics / Inkjet – Printed nanoparticle structures

Flexible electronics could enable new classes of devices towards the improvement of major areas of life, such as renewable energy sources, medical diagnostics, food safety monitoring, informatics, and other systems. There is a growing interest in the development and production of flexible electronic devices [1], photovoltaic cells, gas sensors [2], batteries [3], wearable devices [4], information displays and other systems [5]. The increasing demand for flexible electronics across varied application sectors is expected to drive the market growth significantly over the next few years.
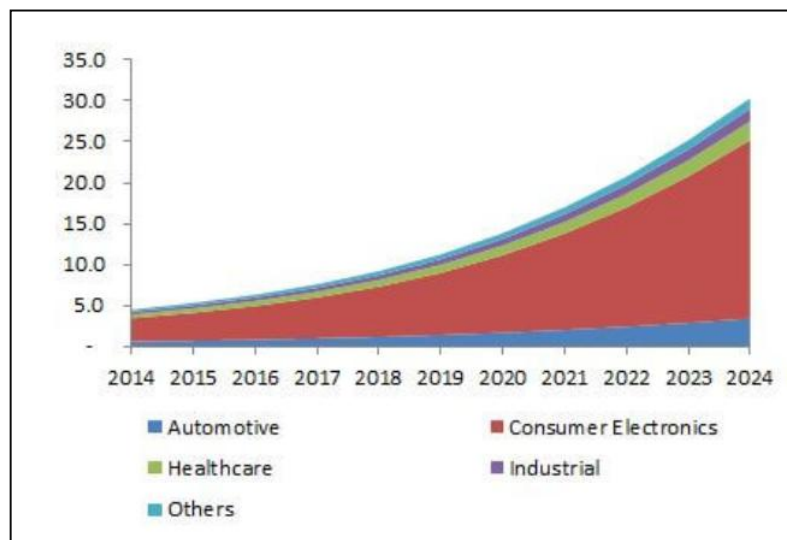
Figure1.1: Global flexible electronics market, by application, 2014 – 2024 (USD Billion)
[Source: https://www.ameriresearch.com]

Flexibility, portability, robustness are some of the attributes of flexible electronics that make this technology attractive to product designers and consumers. As the production of flexible devices escalates, arouses the demand for low cost and fast process of high-performance flexible electronics. A flexible electronic device typically contains several key components, including the substrate, the active layer, and the interface layer. A generic electronic structure is composed of a substrate, electrodes, a front-plane, and encapsulation. To make the structure flexible, all components must comply with bending to some degree without losing their function. Two basic approaches have been employed to make flexible electronics: a) transfer and bonding of completed circuits to a flexible substrate and b) fabrication of the circuits directly on the flexible substrate [6]. Lithography was the main strategy to develop this kind of devices. During the last decades Laser Sintering technique (Inkjet printing of various materials) has emerged as one of the key techniques for electronics' manufacturing and has been established as a reliable and minimally invasive process, compatible with additive manufacturing of electronic devices.
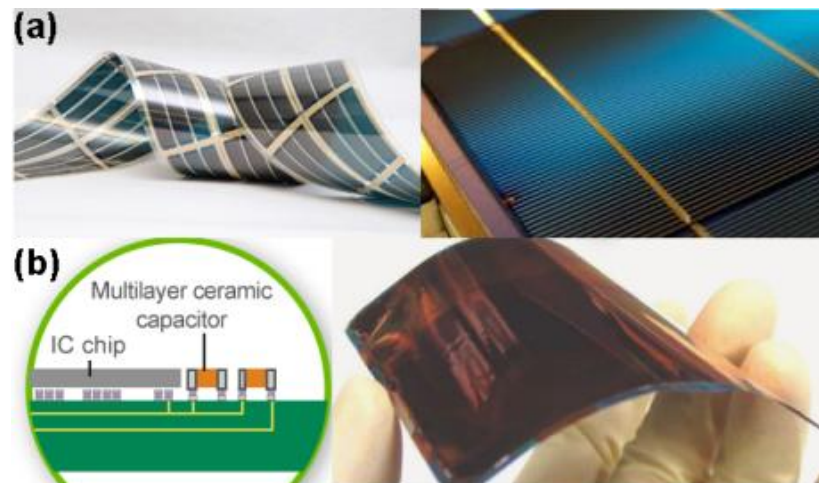
Figure 1.2: Energy applications of flexible inkjet printed devices: a) photovoltaic grid electrodes and b) capacitors

1.2 Sintering methods

1.2.1 Sintering process

Sintering is the terms of the process which makes a powdered /nanoparticle material coalesce into a solid or porous mass by heating it without liquefaction. In this section sintering of inkjet nanoparticle (NPs) structures process is presented.

The processing of NPs ink solutions can be described into three stages [7] Figure 1.2:

- Printing of the desired structures
- Dispersion drying: evaporation of solvent, removal of stabilizers, agglomeration of NPs
- Sintering of the NPs structure: destruction of the coupling of stabilizers with the surface of the particle and their decomposition, coalescence of NPs.
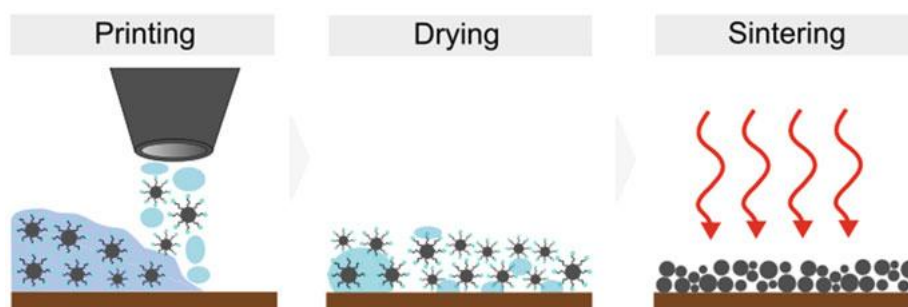
Figure1.3: Processing steps of sintering [7].

Applied energy causes the destruction of solvent remains by thermal dislocation, defined evaporation and partial carbonization. As a result, metal NPs begin to contact. To obtain good electrical characteristics, the solvent and other organic dispersion components should be left to dry before the sintering phase. In some cases low thermal annealing of the printed structure is required. Then diffusion of atoms between NPs can occur. Further aggravation induces the formation of "necks" (Figure1.4) with a subsequent growth of grains, due to which an increase in the compactness of the structure can be observed [8], [9].
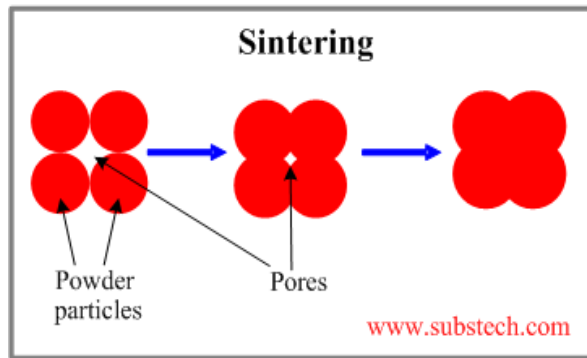
Figure 1.4: Coalescence of powder particles during the sintering process.

The formation of the "necks" between the particles is referred as Solid State Sintering. Solid state sintering is a thermal process that occurs at temperatures between Tm/2 and Tm, where Tm is the melting temperature of the material. Various physical and chemical reactions occur, the most important being diffusion. It involves neck formation (Figure 1.4) between adjacent powder particles. The main driving force for sintering is the lowering of the free energy when particles grow together. A gradient in vacancy concentration between the highly curved neck (high vacancy concentration) and the flat surfaces (low vacancy concentration)causes a flux of vacancies from the neck and a flux of atoms towards the neck thus increasing the neck size. The main advantage of Solid State Sintering is that a wide variety of materials can be processed this way. As long as the temperature is high enough to provide the necessary kinetic energy for the transport of vacancies across the particle boundaries, all powder materials will consolidate via volume diffusion [10].
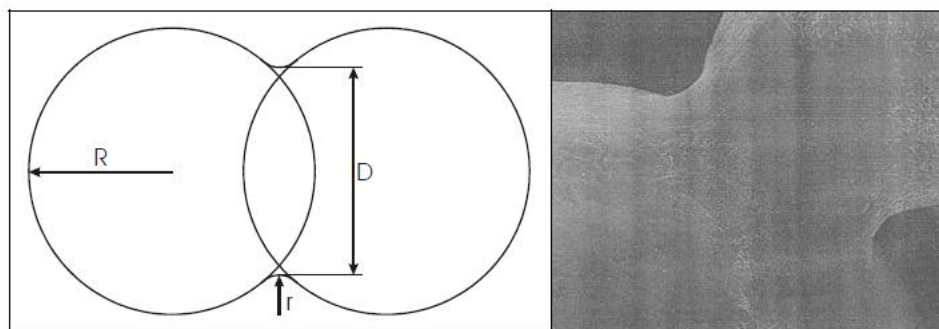
Figure 1.5: Neck formation between two nanoparticles [10].

The sintering process results depend on a large extent on whether applied energy is enough and organic components are actually removed. This obviously becomes more important at relatively low processing temperatures. Using the sintering processes includes facing a contradictory task. On the one hand, the annealing temperature should be sufficient to form a compact structure of the conductive layer, reliable sintering/bonding between the particles to achieve a minimum resistance of the formed conductor. On the other hand, the temperature should not overcome the oxidation temperature in case of metal NPs or damage the substrate [1.10]. Efficient sintering of NPs structures is a key step in the direction of large scale flexible electronics. However the main disadvantage of the technique is the

limited choice of substrates can be used. The efforts to avoid relatively high sintering temperatures are directed to reducing the particle size and selecting organic stabilizers, solvents, and their concentrations.

1.2.2 Sintering techniques

Several sintering approaches have been reported in bibliography. In this paragraph the most important of them are described.

Oven sintering: Using an over to heat nanoparticle structures is one of the simplest and low-cost techniques while can be applied for various types of powders. However, this approach is time-consuming, and cannot be applied to many thermoplastic substrates due to their low glass-transition temperatures (Tg) [7].

Plasma Sintering: This type of sintering can be used both for metallic nanoparticles and for organo-metallic composites on thermally sensitive polymeric substrates. Plasma sintering is based on the effect of the low-pressure argon plasma or the electron-cyclotron resonant (ECR) plasma on the printed structures. Plasma can be used for densification of powder materials, as well as etching and sintering of thermally sensitive materials. Therefore, it can be assumed that such a treatment may be suitable for sintering metal nanoparticles [11], [1.10].

Microwave sintering: Microwave radiation is used to heat metal nanoparticles up to sintering temperatures. In this case, nanoparticles are mixed with electrically conducting powders to enhance the radiation absorbance [12].

Laser sintering: Laser sintering is the technique that employs a laser as the power source to sinter powdered material. This approach is described in Section 1.3.

1.3 Laser sintering

The mechanism of laser sintering of metallic nanoparticles is to a certain extent similar to thermal sintering. In this case absorption of light by printed patterns of metal nanoparticles leads to local heating (photothermal effect), which causes evaporation of the solvent and ligands, and the subsequently sintering of the nanoparticles.

If we consider the case of visible laser irradiation of Silver NPs, the laser deposits energy to the particles to heat them so the process described in Section1.2.1 begins. Nanoparticles of noble metals (e.g. Ag), show a strong absorption in the visible wavelengths. The efficiency of coupling of radiation to NPs depends on the proximity of laser wavelength to plasmon frequency of charge carriers. After the excitation of plasmons, the energy from electrons to the lattice is transferred within 3–5 ps, and the temperature T of the nanoparticles can be estimated on the basis of conventional heat diffusion equation[13]. For successfully sinter the nanoparticles structure, laser irradiation heats up only the surface of the particles to enable the diffusion of the atoms according to the solid state sintering mechanism.
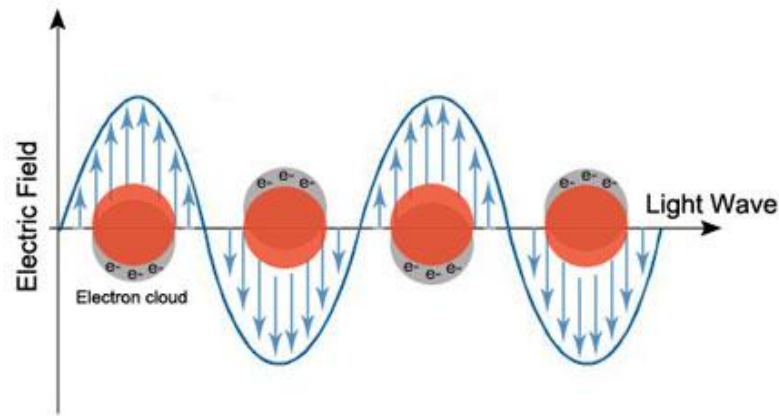
Figure 1.6 Excitation of Plasmons in nanoparticles.

Laser sintering phenomenon is utilized through two approaches. Selective Laser Sintering (SLS) an Laser Sintering of prepared powder patterns. The first is commonly used in industry for the manufacturing of 3D components and the later is preferred in the development of thin film devices and flexible electronics. Different laser sources with various spectral characteristics and power can be used in the process. Both pulsed and continuous wave (CW) laser have been utilized in laser sintering applications. The heat transfer from the heated layer to the cold substrate will obviously lead to an increase in its temperature; however, by applying energy by short pulses, it is possible to avoid overheating and damage of the substrate. This is one of the mail advantages of this technique. Additionally, in both cases the scanning laser beam has the capability to deliver the energy to particular regions so efficient selective energy transfer is achieved while a fully control laser systems has the ability to vary the dose to different areas of the pattern. Comparing the technique with the ones mentioned in Section 1.2.2 it becomes clear that it is the fastest between them. The processing depth when using a laser beam is also limited. Lasers that generate short pulses are commonly used for micromachining and ablation. In both cases, a small zone of thermal influence is decisive, which is also important for the process of selective sintering. High intensity of laser pulses allows achieving greater depth of processing than in the case of continuous wave lasers. Using continuous generation lasers, materials are heated more smoothly, but more heat is transferred to the substrate [7].

2. Problem statement and aim of the present thesis

Digital printing of NPs inks complemented by direct laser sintering enables the mass production of digital conductive and semiconducting patterns, which is advantageous for the performance of existing additive manufacturing technologies in multiple ways.
Among sintering approaches thermal sintering is often used. However, this technology is time-consuming, energetically inefficient and cannot be applied to many thermoplastic substrates due to their sensitivity to temperature. Laser sintering has been demonstrated to be an attractive alternative, allowing a fast and energy efficient process, suitable to be used with temperature sensitive substrates. Several studies on laser sintering have been reported

in literature. Nevertheless, most of them require the utilization of high-cost pulsed lasers systems [14], [15].

The aim of the present study is the development of low-cost and compact CW laser sintering setup. The setup will be used for the sintering of inkjet printed metallic (silver) structures for photovoltaics as well as semiconducting structures (Zinc Oxide).

3. Experimental part : Materials and methods

3.1 Printed Silver (Ag) lines on flexible substrates

3.1.1 Printing of Nanoparticle patterns

Two types of printed nanoparticle patterns were used in the present work, metal and semiconductor. Silver (Ag) nanoparticle patterns were printed by PVnanocell Ltd. of suitable inks for digital inkjet printing by choosing appropriate concentrations of solvents, additives, and NPs content. This ink was used to print Ag nanoparticle structures (lines) of different dimensions on flexible substrates. Kapton films and FR4 was used as substrates. The TCM Group of IESL/FORTH developed a ZnO nanopartile paste and printed patterns (square) on glass substrates.
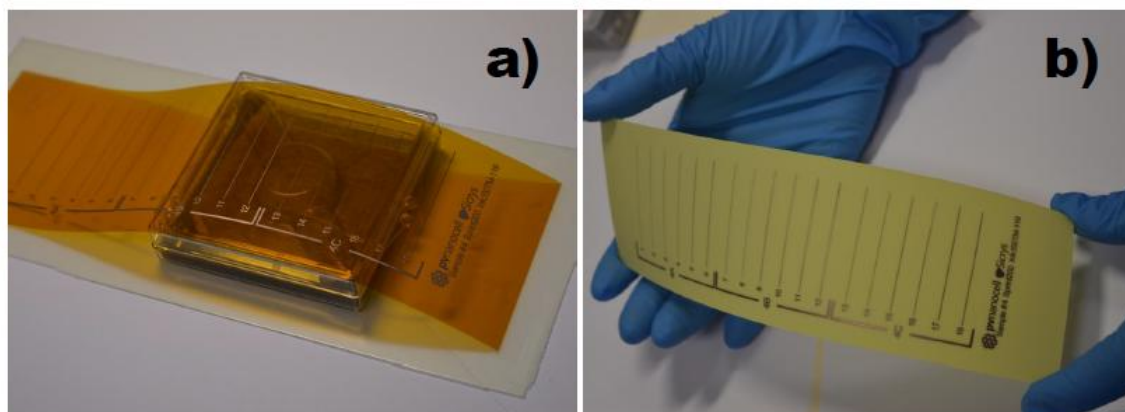
Figures: Samples delivered from PVnanocell: a) Ag lines on Kapton, b) Ag lines on FR4

3.1.2 Kapton substrates

Kapton is a polyimide film developed by DuPont in the late 1960s that remains stable across a wide range of temperatures, from −269 to +400 °C [16]. Kapton is used in, among other things, flexible printed circuits (flexible electronics) and space instruments applications. The chemical name for Kapton K and HN is poly (4,4'-oxydiphenylene-pyromellitimide). It is produced from the condensation of pyromellitic dianhydride and 4,4'-oxydiphenylamine. Kapton is synthesized by the reaction of dianhydride in step polymerization. The intermediate polymer, known as a "poly(amic acid)", is soluble

because of strong hydrogen bonds to the polar solvents usually employed in the reaction. The ring closure is carried out at high temperatures (200–300 °C).
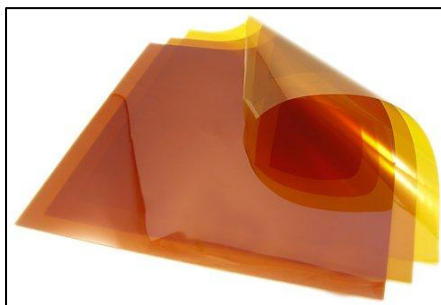

Figure 3.1: Kapton films

3.1.3 FR4 substrates

FR4 is a composite material composed of woven fiberglass cloth with an epoxy resin binder that is flame resistant. FR-4 glass epoxy is a popular and versatile high-pressure thermoset plastic laminate grade with good strength to weight ratios. With near zero water absorption, FR-4 is most commonly used as an electrical insulator possessing considerable mechanical strength. The material is known to retain its high mechanical values and electrical insulating qualities in both dry and humid conditions. These attributes, along with good fabrication characteristics, lend utility to this grade for a wide variety of electrical and mechanical applications. In particular, FR-4 is a common material for printed circuit boards (PCBs) [17].
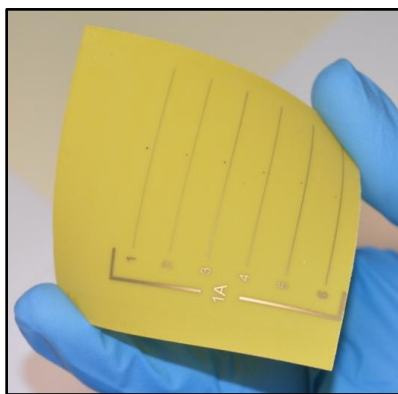
Figure 3.2: FR4 substrates.

3.2 Characterization of the printed Ag lines

In order to investigate whether it is possible to utilize structures produced by the procedure described in the previous paragraph 3.1, we have to characterize them regarding their quality and electrical properties. This will be achieved through the following procedure: Characterization of the morphology of the Silver (Ag) nanoparticle structure before and after the laser treatment to determine whether it has become compact and uniform. Following we measure the conductivity of the structures. A circuit (or an electrical contact)

is a path that electricity flows along. Therefore, it is easily understood that the value of the conductivity of the structure is the key point that makes it a promising candidate for the development of electrical circuits and electrical contacts.

3.2.1 Scanning electron microscopy (SEM)

3.2.1.1 Technique

Scanning electron microscope (SEM) is a type of microscope that uses an electron beam to illuminate the specimen and produce a magnified image. The beam of electrons is produced at the top of the microscope (electron gun), follows a vertical path through the column of the microscope, makes its way through electromagnetic lenses which focus and directs the beam down towards the sample. The beam passes through pairs of scanning coils or pairs of deflector plates in the electron column, typically in the final lens, which deflect the beam in the x and y axes so that it scans over a rectangular area of the sample surface. The focused beam of high energy electrons generates a variety of signals at the surface of solid specimens. The signals that derive from electron-sample interactions reveal information about the sample, including external morphology or surface topography, chemical composition and other properties, such as electrical conductivity. To interact with the bombarded electron beam a conducting surface is necessary. The spatial resolution of SEM depends on the size of the electron spot, which in turn depends on both the wavelength of the electrons and the electron-optical system which produces the scanning beam. Regarding on the resolution it ranges between 1 and 20 nm (depending on the instrument) [22] [N. Cortadellas et al., 2012]

3.2.1.2 Experimental process

Inkjet – Printed nanoparticle structures (lines) on flexible polymer substrates were morphologically characterized by scanning electron microscopy (SEM). SEM characterization was performed on a JEOL 7000 field emission scanning electron microscope with an acceleration voltage of 15 kV. All samples were coated with 10 nm gold prior the characterization using the sputter deposition method in order to make their surface conductive. SEM images are useful to extract conclusions regarding the compactness of the nanoparticle structures.

3.2.2 Conductivity measurements

3.2.2.1 Technique

The electrical conductivity (or resistivity) of the printed conductors has been determined using a simple resistance measurement method.

Electrical conductivity is defined as the reciprocal of resistivity, where the resistivity ρ is defined as:

$\rho = R \cdot A / L$

Where R is the electrical resistance, A is the cross-section area (calculated by multiplying thickness by width), and L is the conductor length Figure 3.5.

3.2.2.2 Experimental process

Metallic contacts were deposited on the Ag nanoparticle lines Figure 3.3. For the contacts was used silver conductive adhesive paste. Resistivity of the lines was measured using a Micro-Ohmmeter.

3.3 Laser sintering of the printed Ag lines

3.3.1 Experimental set-up

A computer controlled laser sintering set-up was developed for the rapid and effective laser treatment of the printed Ag lines.
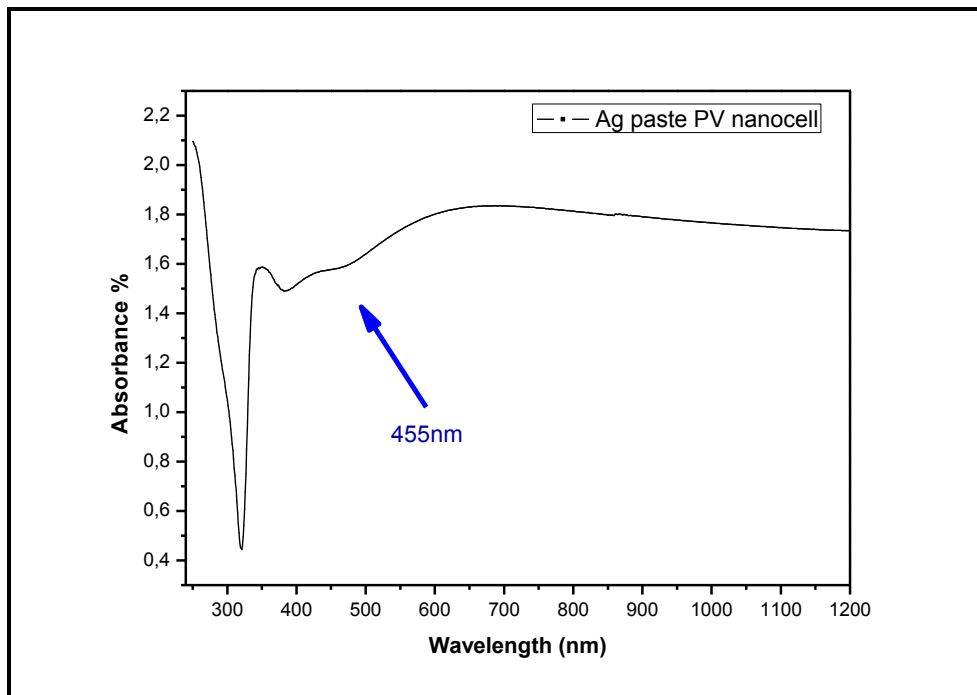
Graph 3.1: Absorbance spectrum of Ag nanoparticle paste.

The experimental set-up is able to truck and irradiate both simple Ag lines and more complex shapes that could be utilized in the development of soft electronics. In addition the setup provides the ability to alternate the optical system and shape the laser beam. Using different beam shapes we can process samples of various size values. Through an easy-to-use software we control the main parameters of the study, the energy of the laser beam and the scanning speed. The following geometry was chosen for the sintering set-up: the sample is stable and a moving head irradiates the samples. This particular geometry allows the irradiation of large samples with maximum stability (minimizing vibrations).

A schematic representation of the experimental setup is shown at the Figure3.6. The head of the setup including the laser source and the focusing lens, is fixed on a rails system which allows the movement across the X-Y plane. It is worth to mention that this type of setup with a moving laser source was chosen due to the significant low cost in contrary with galvo driven laser systems used in laser sintering applications[17]. Sample holder is fixed on a translation stage which can move across Z-axis.
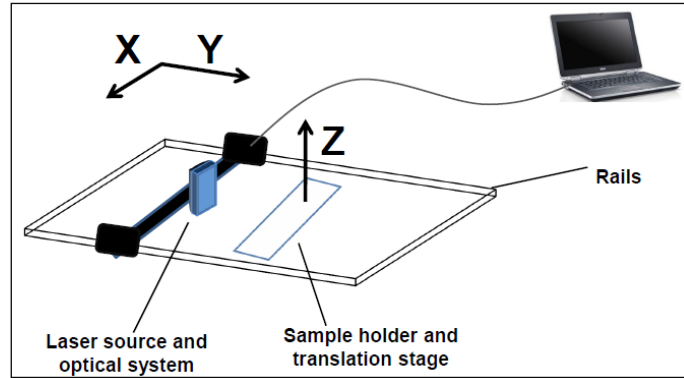

Figure 3.3: Schematic representation of the laser sintering setup.

A 455nm diode laser with a maximum output of 5 Watt is used to irradiate the lines. Absorbance spectrum of Ag nanoparticle paste used for the printing of samples is shown in Graph 3.1. The absorbance at the wavelength of the laser used in the experiments is indicated in the Graph.

A plano-convex optical lens of 2cm focal length focuses the laser beam on the sample surface. In all the experiments, the diameter of the laser beam was less than or equal to the width of the NPs structures. The head moves with an adjustable scanning velocity up to 10cm/s across the X-Y plane.
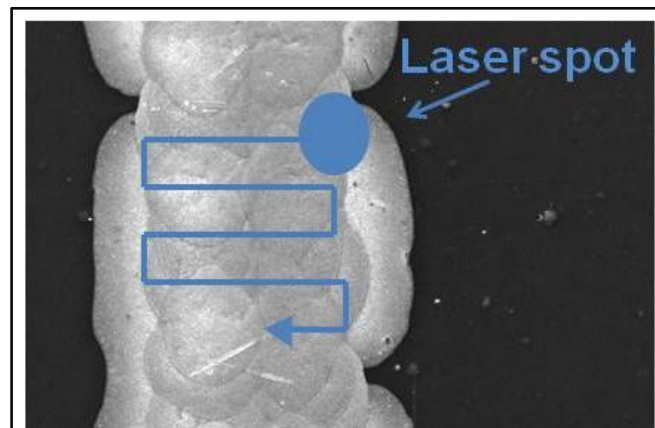

Figure 3.4: Scanning path of the laser.

Regarding the scanning of the Ag lines, two approaches have been used. The first was the parallel scanning of the line. The second was of a rectangle shape track as depicted in Figure3.7. The scanning path of Figure3.4 was chosen for the irradiation of the wider samples. A mini camera is mounted on the moving head, right above the sample, in order to monitor the position of the focused laser beam on samples surface.

The laser sintering setup described above is a compact system that allows fast and fully controllable sintering of printed metal lines.
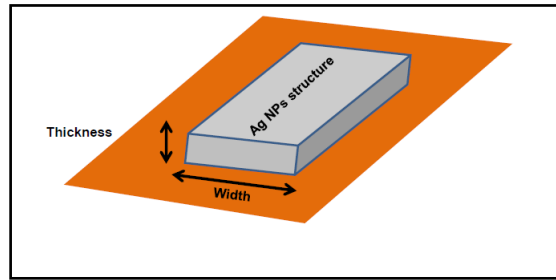

Figure 3.5: Schematic representation of the Ag NPs structure.

3.3.2 Experimental parameters

In the present study we consider the continuous-wave (CW) laser sintering of Silver (Ag) printed lines. Using a low cost CW laser set-up we investigate the two main parameters: laser irradiance applied on the nanostructures and scanning speed. Furthermore two different scanning paths are used to scan the surface of the structures.

4. Results

Following the laser irradiation of the samples, the sintering performance will be tested by morphological and electrical characterization of the sintered Ag patterns in order to compare the effectiveness of the CW laser sintering method with respect to the oven sintering one.

In this Chapter, the experimental results from the laser sintering experiments outlined in Section 3.3 are presented and examined in detail. The effects of the main experimental variables on the resulting specific resistance of the laser-treated Silver (Ag) NPs lines are shown in the tables of Section 4.1. The surface topography of Ag lines and ZnO structures was analyzed, prior and following the laser treatment, by Scanning Electron Microscopy (SEM). X-ray diffraction analysis (XRD) was performed for further investigation of the Ag NPs structure.

4.1 Conductivity measurements

The specific resistance measured for all the sintered samples prepared is presented in Graphs 1-8. In these graphs the x-axis represents the applied Irradiance, the y-axis the scanning speed and the z-axis represents the resulting specific resistance expressed as a multiple of the bulk conductivity ($\rho_{bulk\ silver} = 1.59 \mu\Omega*cm$). The specific resistance value is expressed as a multiple of the bulk specific resistance to facilitate comparison of the Ag NPs structure with the bulk silver. Each experimental point on the graphs corresponds to a value of the ρ measured, expressed in a "X $\rho_{bulk\ silver}$" form. In all graphs the x - y plane is

placed at the point of z axis, which is equal to the specific resistance value measured after oven sintering. The closer the values of specific resistance are to the x - y level, the closer we get to our goal, to reach the values obtained via oven sintering.

During the experimental process we tuned the parameters and then we performed the characterization of the Ag lines. Nevertheless some parameters were varied over a narrow range of values due to the limited number of samples available (some values are presented with different symbols as explained below). The specific resistance ρ measurements were performed using the simple method described in Section 3.2.2. Therefore ρ is calculated using the equation: $\rho = R*A / L$, where R: measured resistance, L: length of the specimen. The error of the specific resistance measurements wree calculated via error propagation theory. We set a variable $k = A / L$. Then the error of k amount is calculated, using the standard deviation rule, as:

$$\Delta k = k[(\Delta A/A)^2 + (\Delta L/L)^2]^{1/2} .$$

Using the same method the error of specific resistance is:

$$\Delta\rho = \rho[(\Delta k/k)^2 + (\Delta R/R)^2]^{1/2} , \text{ where } \Delta A, \Delta L, \Delta R \text{ are the instrumental errors.}$$

The errors calculated were orders of magnitude smaller than the specific resistance values, hence error bars are smaller than the corresponding symbols' size shown in the graphs. Each of the following graphs corresponds to a sample of different cross section area as described in Section 3.1.

4.1.1 Silver NPs lines on kapton

The laser sintering parameters used, as well as the resulting specific resistance (ρ) values for all the Ag NPs lines on Kapton samples prepared, are shown in the following. The experimental parameters as well as the resulting specific resistance for samples of A= $325.3\mu m^2$ cross section are shown in Table1.

Sample Ag on Kapton of A= 325.3 μm^2 (Width: 133.56μm, Thickness: 2.4μm)

Irradiance (W/cm^2)	Scanning speed (mm/s)	Specific Resistance (μΩ*cm) A= 325.3 μm^2	X $\rho_{bulk\ silver}$
180	4	81.64	51.3
262	4	36.42	22.9
400	4	21.74	13.7
500	4	27.86	17.5
400	2	13.81	8.7
400	6	17.22	10.8

Table 1: Experimental parameters and results for samples with a cross section A= 325.3μm^2.
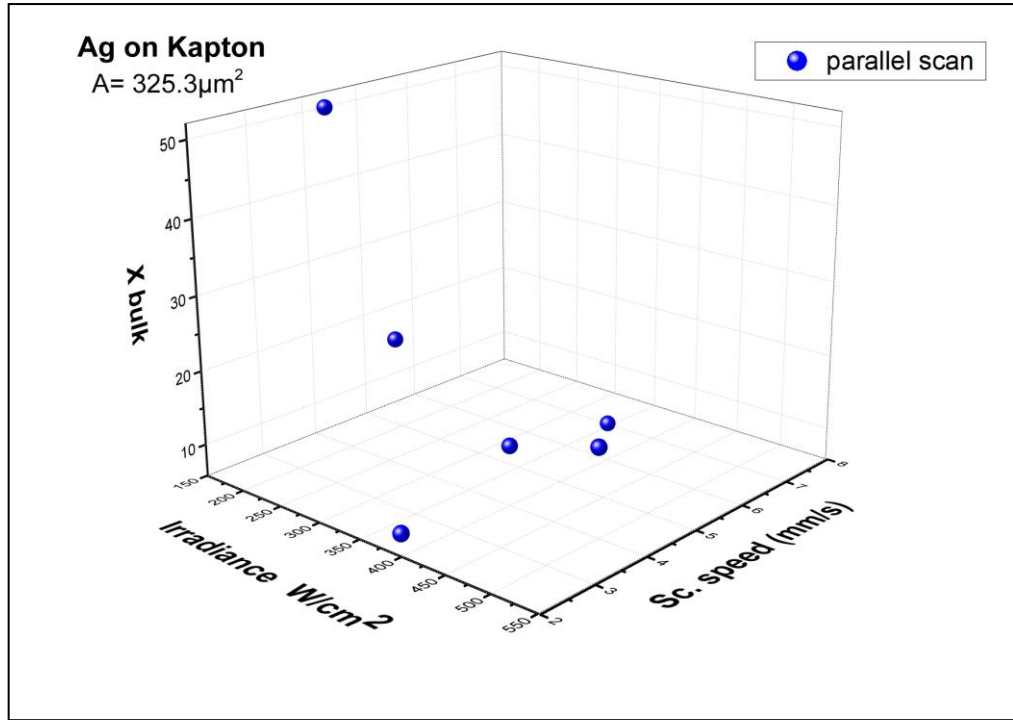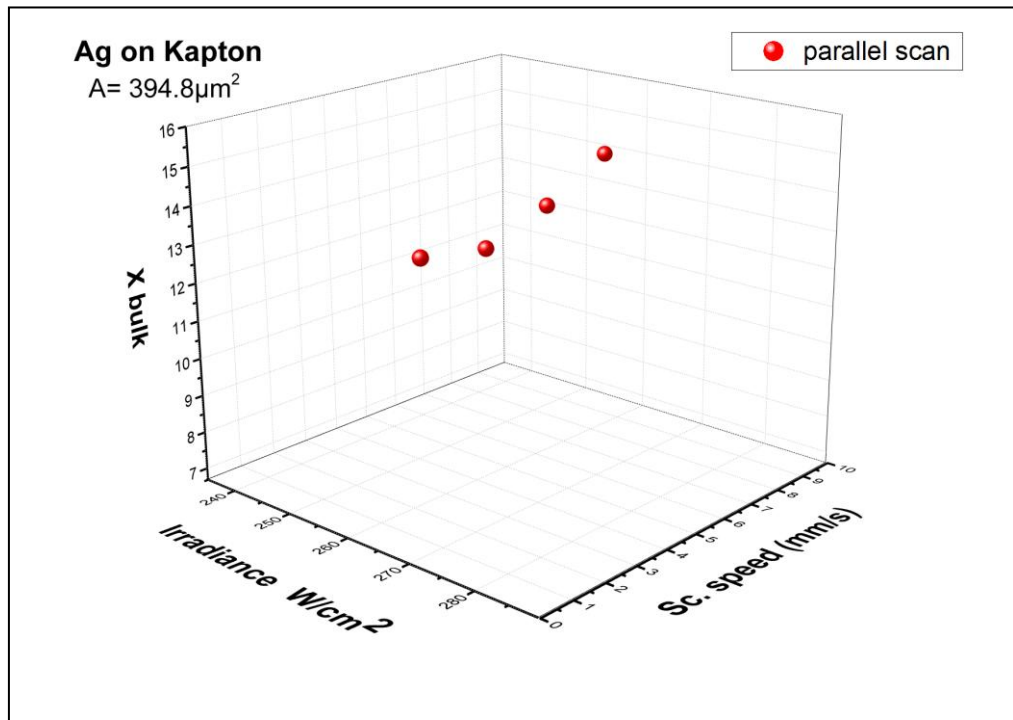
Graph 1: Specific resistance following the CW laser sintering.

As shown in Graph1 the sheet resistance becomes lower as the Irradiance increases up to a value of 400W/cm^2, regardless the scanning velocity 4mm/s and then again increases. This is a well-known behavior in the literature attributed to the fact that for Irradiance values exceeding a critical one, the sample is damaged and therefore specific resistance increases rapidly[18]. Applying different values of Scanning speed we obtained the lowest value of **ρ = 8.7•ρ$_{bulk\ silver}$** which is close to the value of the oven sintering, i.e. (ρ$_{os}$= 5.7•ρ$_{bulk\ silver}$).

The experimental parameters as well as the resulting specific resistance for samples of A= 394.8μm^2 cross section are shown in Table2.

Sample Ag on Kapton of A= 394.8 μm^2 (Width: 158.55μm, Thickness: 2.49μm)

Irradiance (W/cm^2)	Scanning speed (mm/s)	Specific Resistance (μΩ*cm) A= 394.8 μm^2	X ρ$_{bulk\ silver}$
262	2	21.16	13.3
262	4	20.63	13
262	6	21.58	13.6
262	8	23.01	14.5

Table 2: Experimental parameters and results for samples with a cross section of A= 394.8 μm^2.

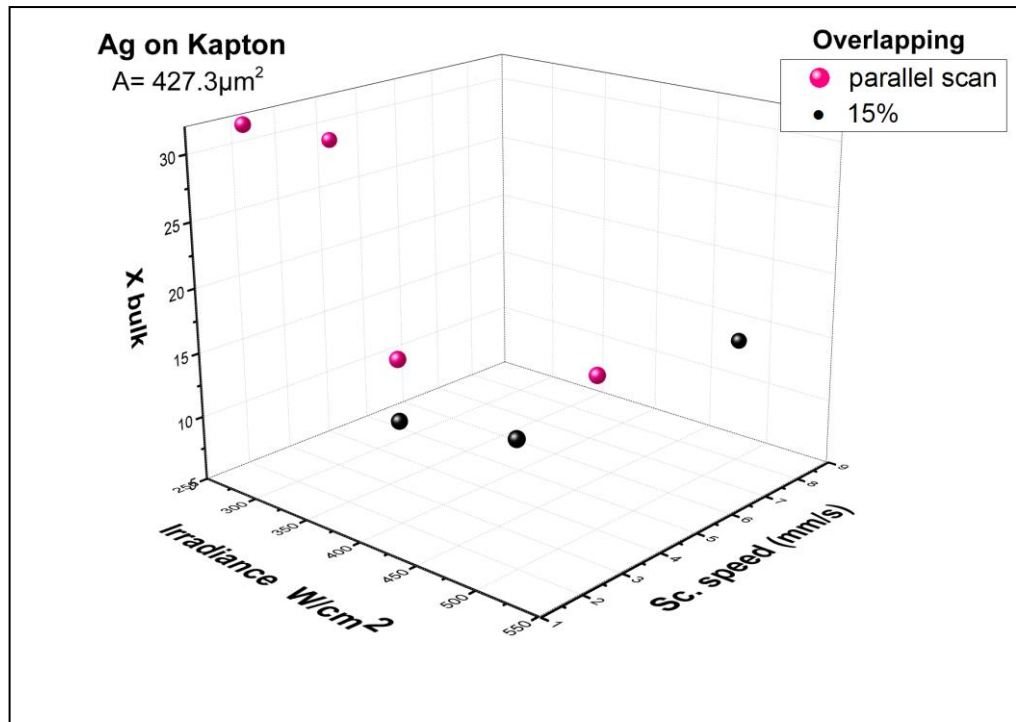**Graph 2**: Specific resistance following the CW laser sintering.

As can be observed in Graph2 that for an Irradiance value of 262 W/cm^2 we obtained the lower value, $\boldsymbol{\rho = 13 \cdot \rho_{\textbf{bulk silver}}}$ for Scanning speed 4mm/s. This value was twice the one measured following oven sintering, i.e. $\rho_{os} = 6.7 \cdot \rho_{bulk\ silver}$.

The experimental parameters as well as the resulting specific resistance for samples of A= 427.3μm^2 cross section are shown in Table3.

Sample Ag on kapton of A= 427.3 μm^2 (Width: 168.9μm, Thickness: 2.53μm)

Irradiance (W/cm^2)	Sc. speed (mm/s)	S. Resistance (μΩ*cm) A= 427.3 μm^2	X ρ$_{bulk\ silver}$	Overlapping %
262	2	50.3	31.6	single scan
400	2	27.6	17.4	single scan
262	4	46	28.9	single scan
500	4	26.4	16.6	single scan
400	2	20.39	12.8	15
500	2	23.03	14.5	15
500	8	23.2	14.6	15

Table 3: Experimental parameters and results for sample of A= 427.3μm^2 cross section.
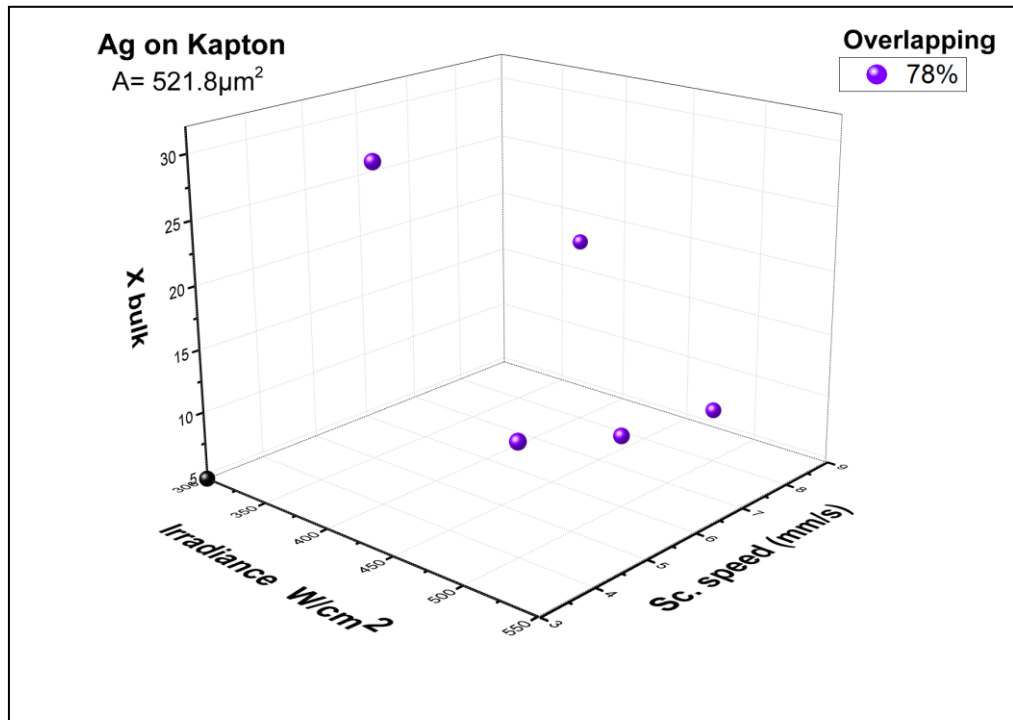
Graph 3: Specific resistance after CW laser sintering.

The corresponding results for samples of A=427.3μm^2 are shown in Graph2. It is obvious that in this case, upon using the rectangle path described in Section 3.3.1, we obtain lower values for the specific resistance. Specifically, for an Irradiance of 400W/cm^2 with an 15% overlap at a scanning speed 2mm/s we measured **ρ = 12.8•ρ$_{bulk\ silver}$.** The corresponding value measured following the oven sintering was ρ$_{os}$= 5.1•ρ$_{bulk\ silver}$.

The experimental parameters as well as the resulting specific resistance for samples of A= 521.8 μm^2 cross section are shown in Table 4.

Sample Ag on kapton of A= 521.8 μm^2 (Width: 209.54μm, Thickness: 2.49μm)

Irradiance (W/cm^2)	Sc. speed (mm/sec)	S. Resistance (μΩ*cm) A= 521.8 μm^2	X ρ$_{bulk\ silver}$	Overlapping %
400	4	48.76	30.7	78
400	8	31.23	19.6	78
500	4	21.15	13.3	78
500	6	16.22	10.2	78
500	8	14.08	8.8	78

Table 4: Experimental parameters and results for sample of A= 521.8μm^2 cross section.
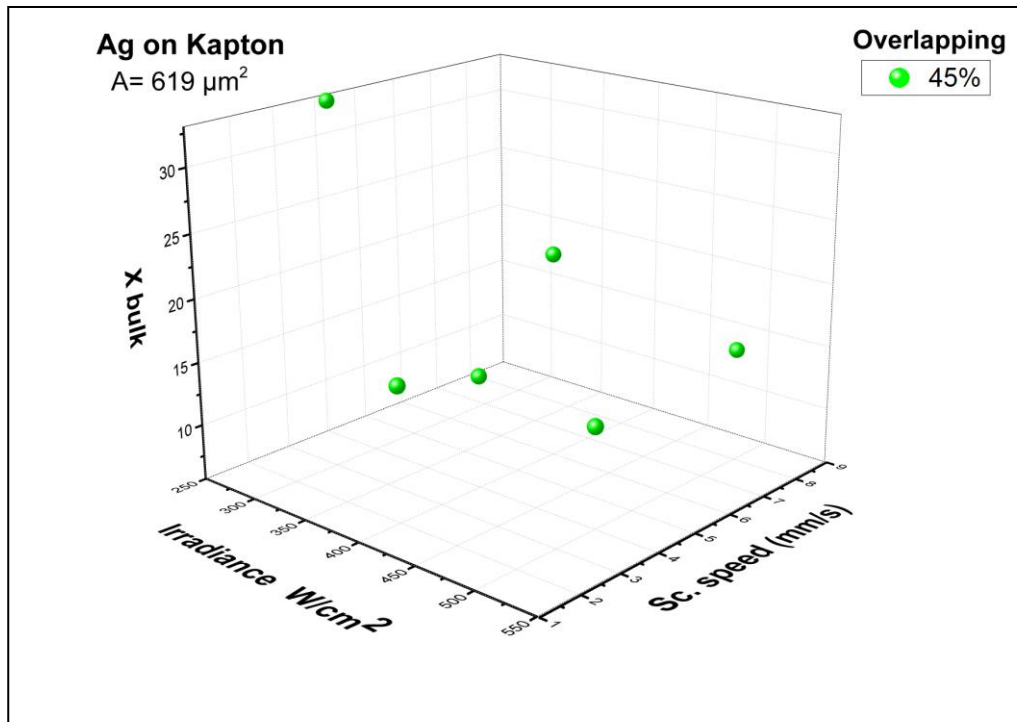
Graph 4: Specific resistance after CW laser sintering.

The application of the rectangle shape laser track in Samples of A= $521.8\mu m^2$ cross section leads to the results of Table 4. The lowest resulting specific resistance value was $\rho =$ **8.8•$\rho_{bulk\ silver}$** following irradiation with 500W/cm^2 with an 78% overlapping at Scanning speed 8mm/s, while the value measured following oven sintering was ρ_{os}= 4.5•$\rho_{bulk\ silver}$.

The experimental parameters as well as the resulting specific resistance for samples of A= $619\mu m^2$ cross section are shown in Table 5.

Sample Ag on kapton of A= 619 μm^2 (Width: 214.19 μm, Thickness: 2.89 μm)

Irradiance (W/cm^2)	Sc. speed (mm/sec)	S. Resistance ($\mu\Omega$*cm) A= 619 μm^2	X $\rho_{bulk\ silver}$	Overlapping %
262	4	52.3	32.9	45
400	2	25.7	16.1	45
400	4	23.1	14.5	45
400	6	34.85	21.9	45
500	4	21.52	13.5	45
500	8	23.2	14.6	45

Table 5: Experimental parameters and results for sample of A= $619\mu m^2$ cross section.

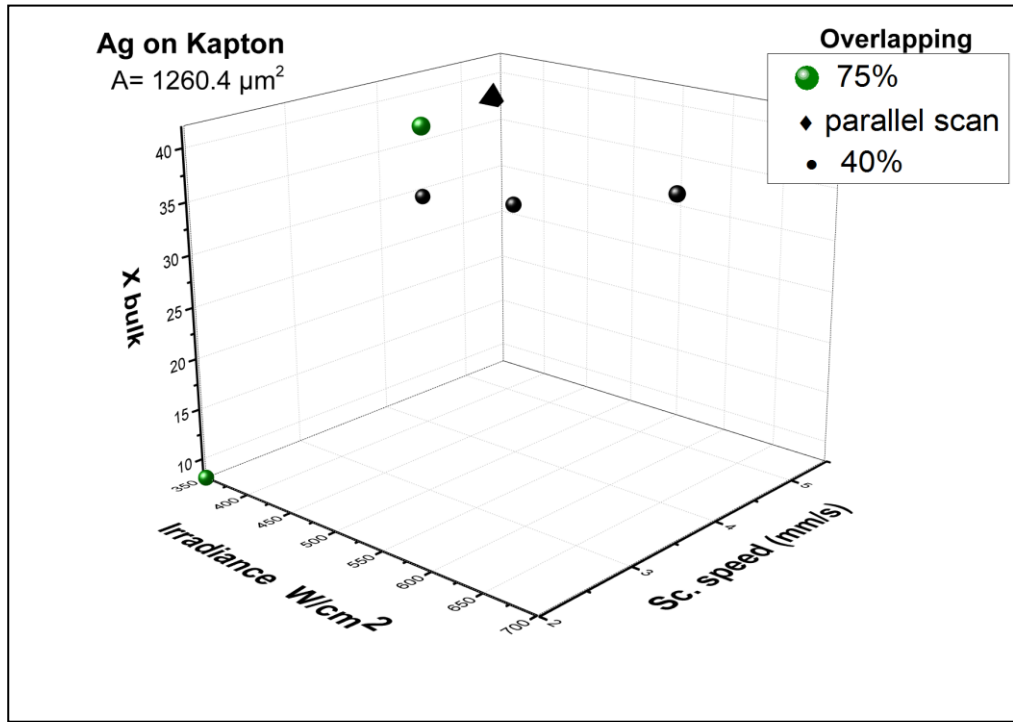**Graph 5**: Specific resistance after CW laser sintering.

As can be observed in Graph5 the application of 45% overlap and different values of Irradiance and Scanning speed give rise to a lowest resulting specific resistance value of **$\rho = 13.5 \cdot \rho_{\text{bulk silver}}$**, which is greater than twice the value measured after the oven sintering, $\rho_{os} = 5.4 \cdot \rho_{\text{bulk silver}}$.

The experimental parameters as well as the resulting specific resistance for samples of A= 1260.4μm^2 cross section are shown in Table 5.

Sample Ag on kapton of A= 1260.4 μm^2 (Width: 151.86 μm, Thickness: 8.3 μm)

Irradiance (W/cm^2)	Sc. speed (mm/sec)	S. Resistance (μΩ*cm) A= 1260.4 μm^2	X $\rho_{\text{bulk silver}}$	Overlapping %
400	4	61.18	38.5	75
400	4	50.08	31.5	40
480	4	67.73	42.6	singe scan
500	4	52.3	32.9	40
660	4	59.45	37.4	40

Table 1: Experimental parameters and results for sample of A= 1260.4μm^2 cross section.

Graph 6: Specific resistance after CW laser sintering.

These were the samples of the largest cross section among those considered in the present study. All specific resistance values we measured in this case were far above those from oven sintering. The lowest resulting specific resistance value was $\rho = 31.5 \cdot \rho_{\text{bulk silver}}$ following irradiation with 400W/cm^2 with an 40% overlapping at Scanning speed 4mm/s, while the value measured after the oven sintering was $\rho_{os} = 8.3 \cdot \rho_{\text{bulk silver}}$.

### 4.1.2 Silver NPs lines on FR4

Laser sintering parameters and the resulting specific resistance (ρ) for all the Ag NPs lines on FR4 substrates samples are shown in following pages.

Sample Ag on FR4 of A= 240.8 μm^2 (Width: 159.5 μm, Thickness: 1.51 μm)

Irradiance (W/cm^2)	Sc. speed (mm/sec)	S. Resistance (μΩ*cm) A= 240.8 μm^2	X $\rho_{\text{bulk silver}}$	Overlapping %
400	4	22.48	14.4	78
500	2	15.79	9.9	78
500	4	18.27	11.5	78
500	6	20.5	12.9	78
500	8	25.3	15.9	78
500	4	18.18	11.4	45

**Table 2**: Experimental parameters and results for sample of A= 240.8μm^2 cross section.
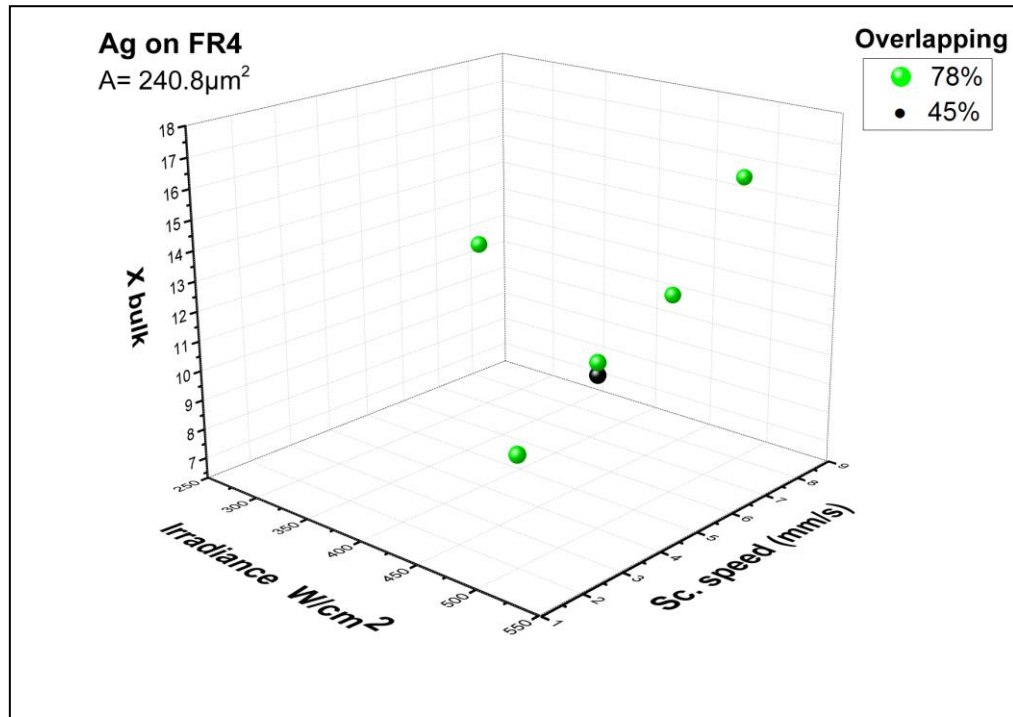
Graph 7: Specific resistance after CW laser sintering.

Applying the rectangle shape track laser irradiation for the Samples of A= 240.8μm^2 we got the results of Table 7. The lowest resulting specific resistance value was **ρ = 9.9•ρ$_{bulk}$ $_{silver}$** after irradiation with 500W/cm^2 with an 78% overlapping at Scanning speed 2mm/s, while the value measured after the oven sintering was ρ$_{os}$= 6.3•ρ$_{bulk\ silver}$.

Sample Ag on FR4 of A= 525.5 μm^2 (Width: 88.61 μm, Thickness: 5.93 μm)

Irradiance (W/cm^2)	Sc. speed (mm/sec)	S. Resistance (μΩ*cm) A= 525.5 μm^2	X ρ$_{bulk\ silver}$	Overlapping %
200	1	49.49	31.1	78
200	2	54.3	34.2	78
300	2	36.04	22.7	78
300	4	41.2	25.9	78
300	8	50.45	31.7	78

Table 8: Experimental parameters and results for sample of A= 525.5μm^2 cross section.
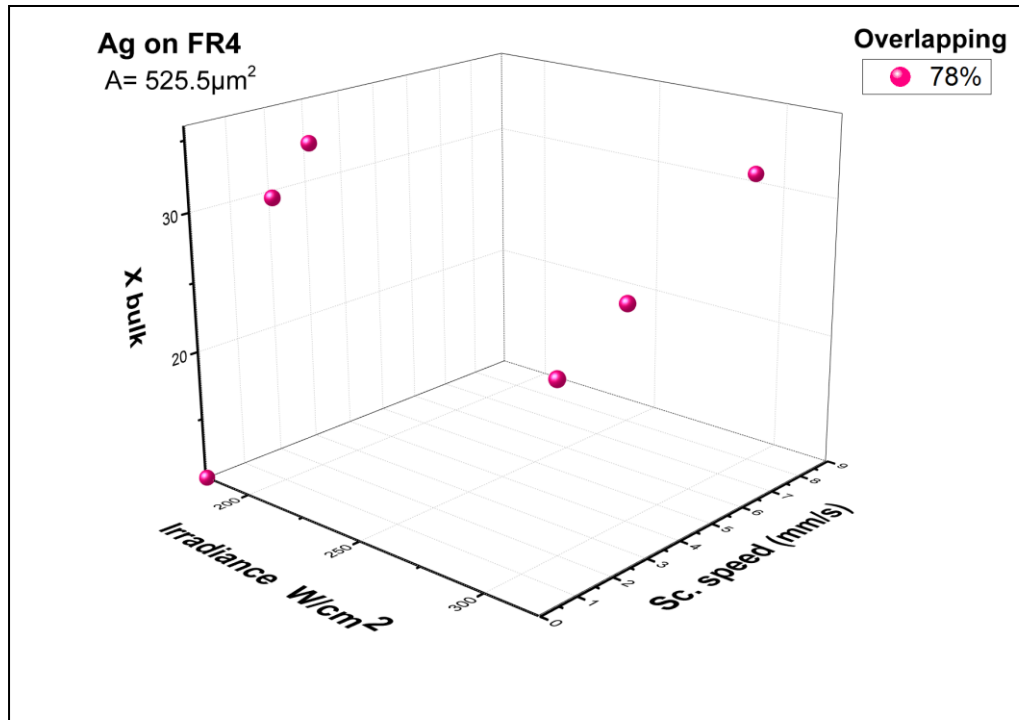
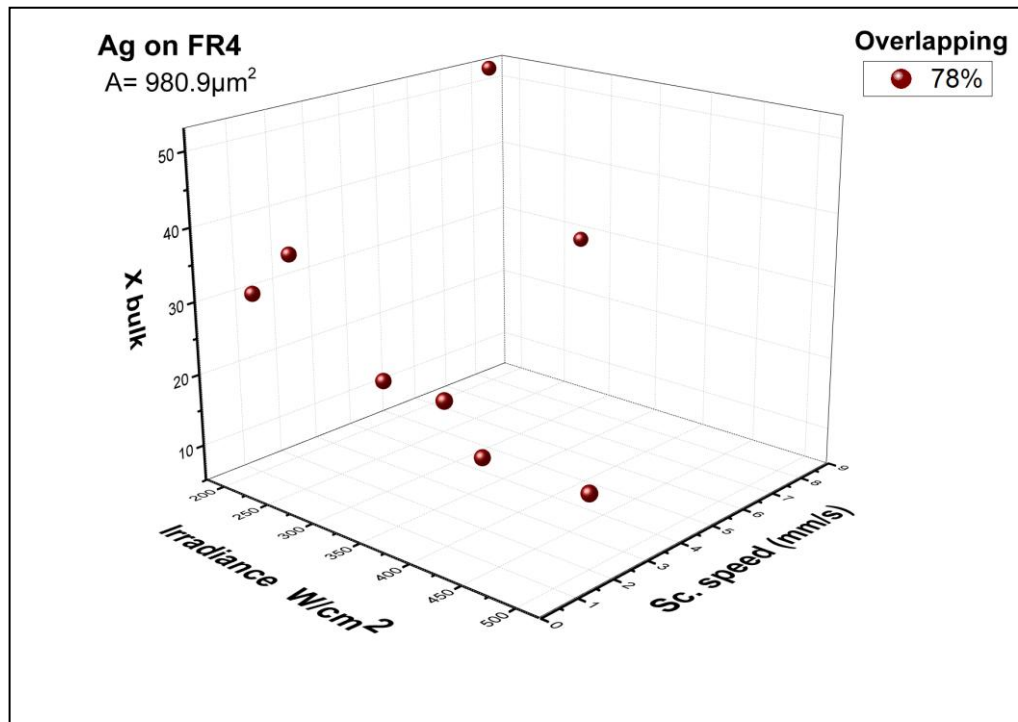**Graph 8**: Specific resistance after CW laser sintering.

Samples of A=525.5µm^2 cross section were irradiated with a rectangle shape track of 78% overlapping. Results are shown in Table 8. The lowest resulting specific resistance value was **ρ=22.7•ρ$_{bulk\ silver}$** after irradiation with 300W/cm^2 with an 78% overlapping at Scanning speed 2mm/s, while the value measured after the oven sintering was ρ$_{os}$=10.5•ρ$_{bulk\ silver}$.

Sample Ag on FR4 of A= 980.9 μm^2 (Width: 159.5 μm, Thickness: 6.15 μm)

Irradiance (W/cm^2)	Sc. speed (mm/sec)	S. Resistance (μΩ*cm) A= 980.9 μm^2	X ρ$_{bulk\ silver}$	Overlapping %
200	2	54.25	34	78
300	2	32.59	20.5	78
400	2	23.4	14.7	78
500	2	23.9	15	78
200	8	83.7	52.6	78
300	8	78.5	30.5	78
200	1	48	30.2	78
400	1	38.5	24.2	78

Table 9: Experimental parameters and results for sample of A= 980.9µm^2 cross section.

Graph 9: Specific resistance after CW laser sintering.

Samples of A=980.9μm^2 cross section were irradiated with a rectangle shape track of 78% overlapping. Results are shown in Table 9. The lowest resulting specific resistance value was **ρ=14.7•ρ$_{bulk\ silver}$** after irradiation with 400W/cm^2 with an 78% overlapping at Scanning speed 2mm/s. This value is three times greater than the oven sintering result which was ρ$_{os}$=5.1•ρ$_{bulk\ silver}$. Specific resistance results will be further discussed in Chapter5.

4.2 Scanning electron microscopy (SEM) images

The printed NPs structures, Ag lines on flexible polymer substrates and ZnO structures on glass, were morphologically characterized by scanning electron microscopy (SEM). SEM is the most useful technique for the study of the surface morphology of nanostructured materials. In case of laser sintering of NPs structures considered in the present study, SEM is able to provide information regarding the effect of the irradiation on the NPs and therefore the efficiency of the sintering technique. Furthermore we can have a general overview of both the NPs structure and the substrate after the laser irradiation to ensure the non-destructive character of the CW laser sintering method.

4.2.1 Silver nanoparticle lines on kapton/FR4

For Ag NPs structures, efficient sintering means that the Ag NPs begin to make physical contact with each other and form a continuous percolating network in the printed pattern. In this section SEM images of both unirradiated and irradiated NPs samples are shown. The effect of laser irradiation on the morphology is considered for three cases, low ρ value, relatively high ρ value and non-conductive irradiated samples, as well as two ZnO structures.
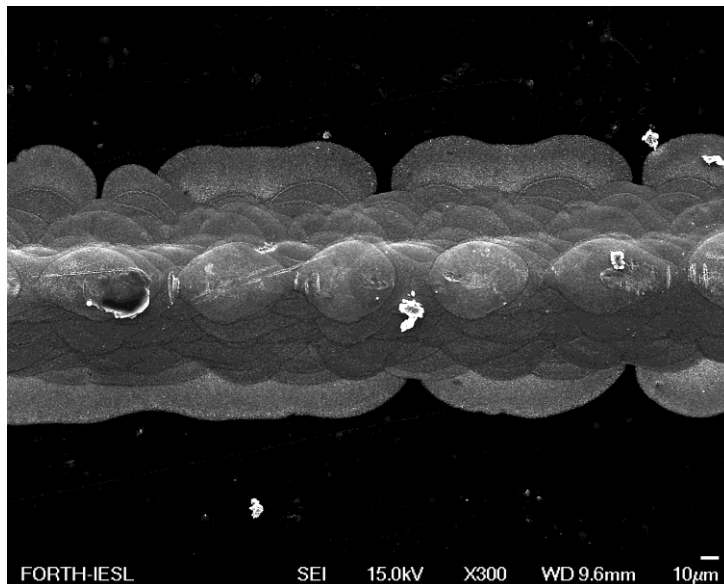

Figure 4.2: SEM image of unirradiated Ag line on kapton.

Figure 4.1 and 4.2 show macroscopic SEM images of the surface of the samples before and after the laser treatment respectively. In Figure 4.2 the sample has been irradiated parallel to the Ag line. We can observe the effect of the focused laser beam on its surface (similar to that has been observed in bibliography [19]), while the substrate around the nanoparticles remains intact.
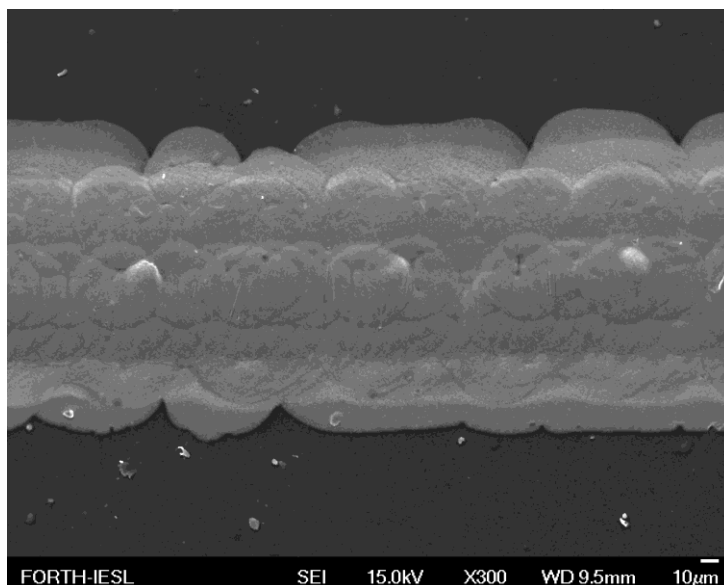

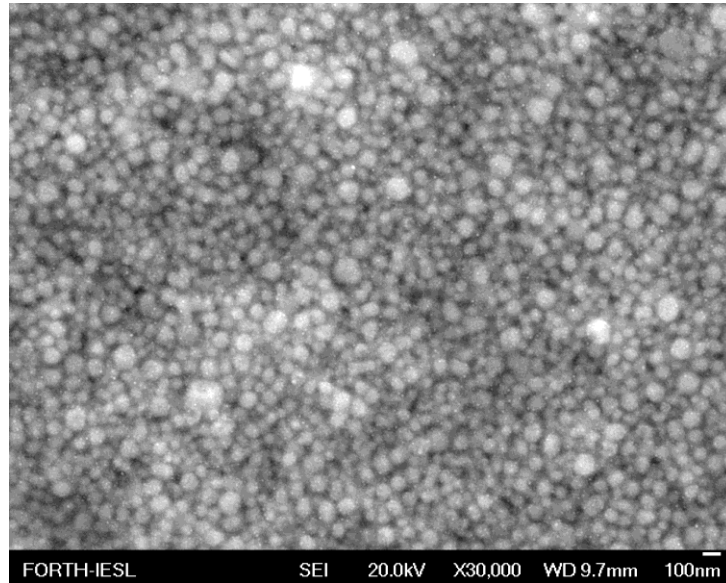**Figure4.3**: SEM image of laser irradiated Ag line on kapton.

Figure 4.3: SEM image unirradiated non-conductive Ag NPs structure on kapton.
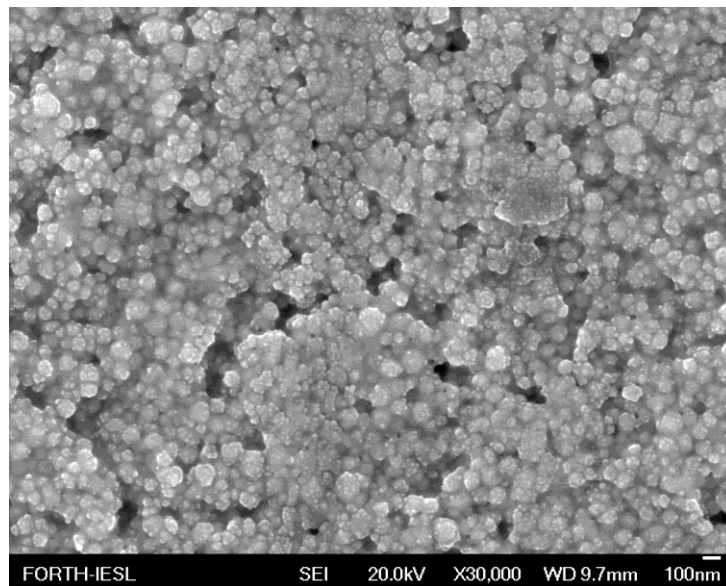

Figure 4.4: SEM image of Ag NPs structure with $\rho = 19.6 \cdot \rho_{\text{bulk silver}}$

In Figure 4.4 the sample ($A = 521.8 \mu m^2$) has been irradiated applying $400W/cm^2$, 8mm/s, 78% overlapping and its specific resistance was measured $\mathbf{\rho = 19.6 \cdot \rho_{bulk\ silver}}$ after the laser sintering process.
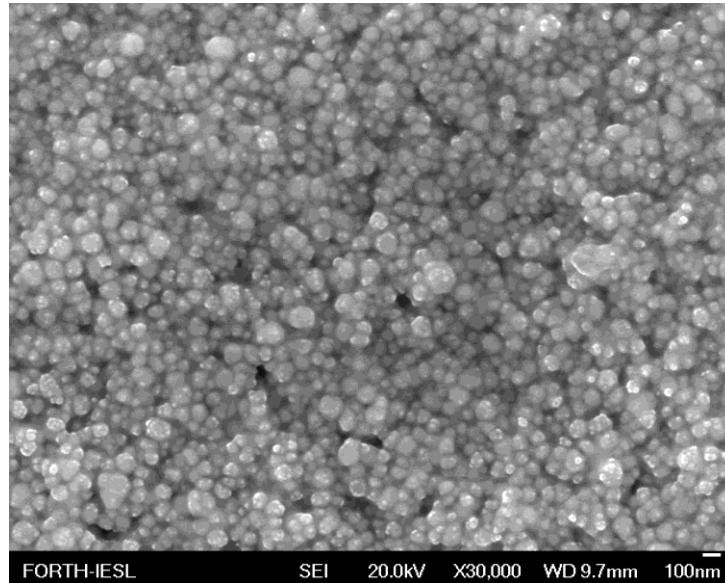
Figure 4.5: SEM image of Ag NPs structure with $\rho=8.8 \cdot \rho_{\text{bulk silver}}$.

In Figure 4.5 the sample ($A=521.8\mu m^2$) has been irradiated applying $500W/cm^2$, 8mm/s, 78% overlapping and the specific resistance was measured $\boldsymbol{\rho=8.8 \cdot \rho_{\text{bulk silver}}}$ after the laser sintering process.
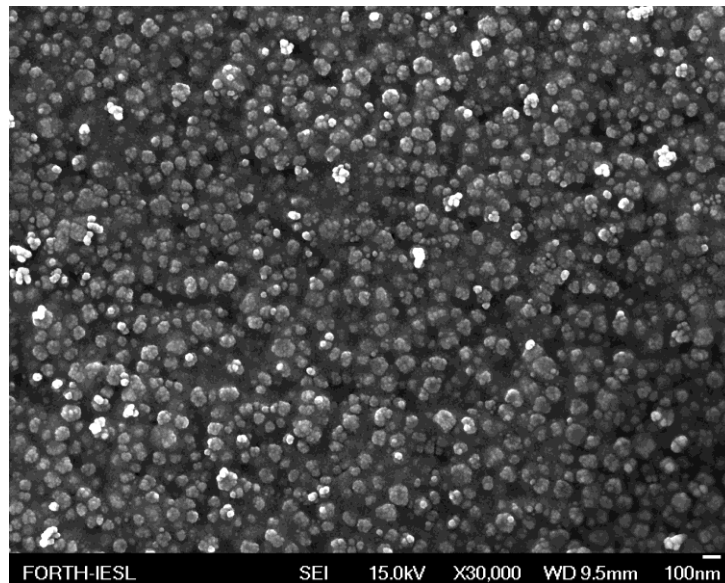

Figure 4.6: SEM image of non-conductive Ag NPs structure.

In Figure 4.6 the sample has been irradiated applying $700W/cm^2$, 8mm/s, 78% overlapping and was non-conductive after the laser sintering process.

It is observed at the cases of Figures 4.4-4.6 that an increase of the compactness has occurred after the laser irradiation as "necks" have been formed between the Ag NPs. Also we can observe the formation of larger particles.
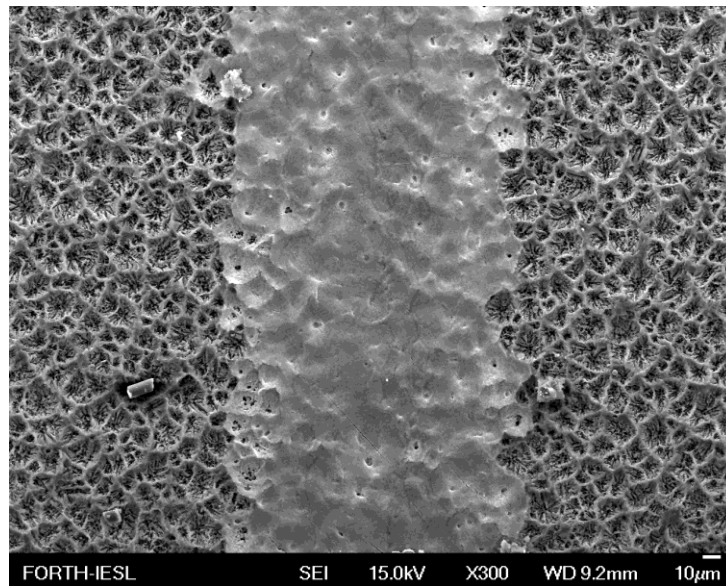
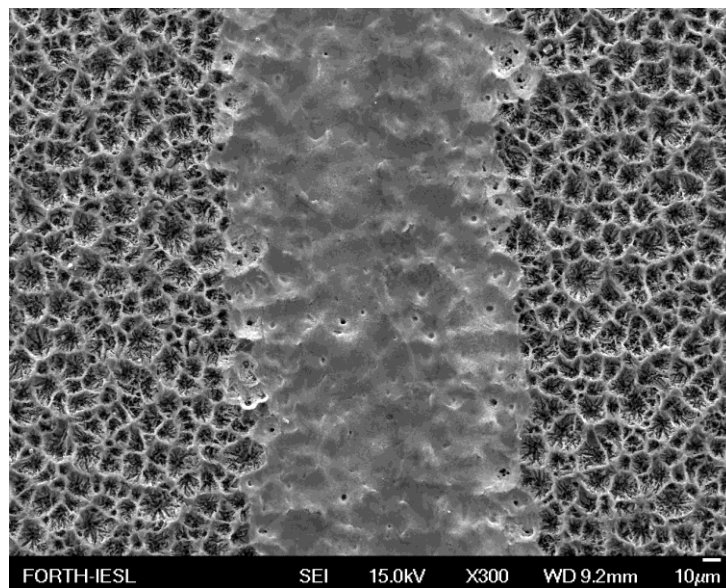**Figure 4.7**: SEM image of unirradiated Ag line on FR4.

Figure 4.8: SEM image of laser irradiated Ag line on FR4.

Figure 4.7 and 4.8 show macroscopic SEM images of the surface of the samples before and after the laser treatment respectively. In Figure 4.2 the sample has been irradiated but there is no observable modification of the structure surface at this microscope magnification. Also the substrate around the nanoparticles remains intact.
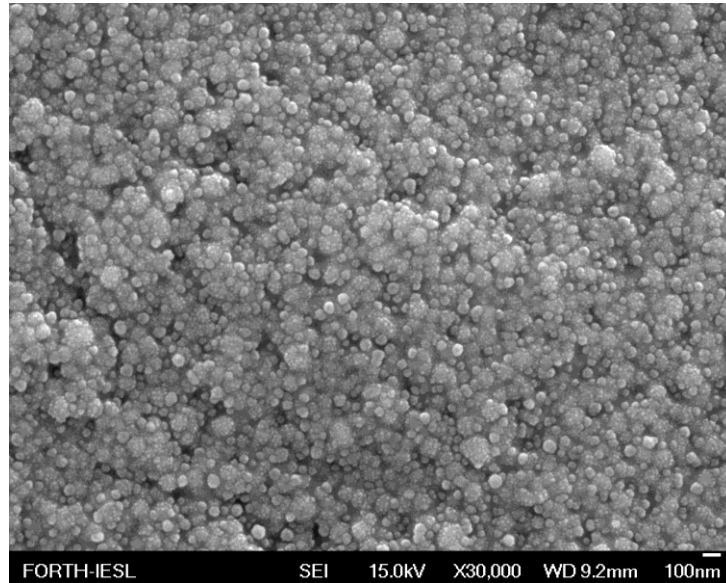
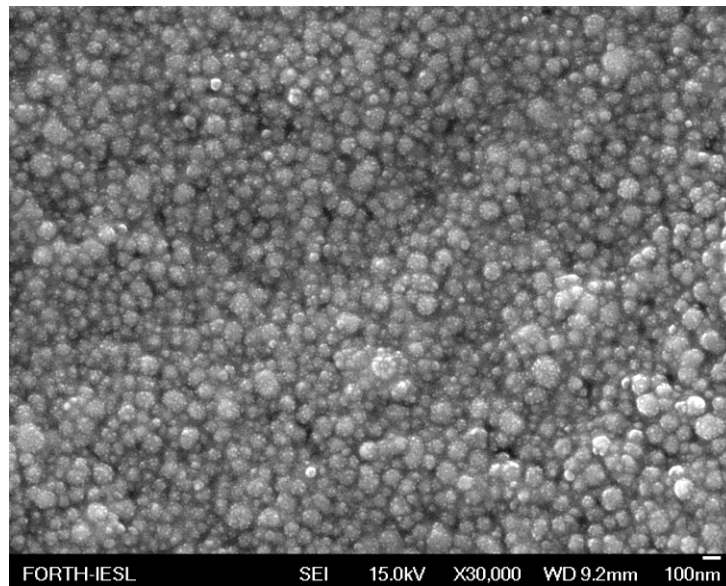**Figure 4.9**: SEM image unirradiated non-conductive Ag NPs structure on FR4.

Figure 4.10: SEM image of Ag NPs structure with $\rho=14.7 \cdot \rho_{\text{bulk silver}}$.

In Figure 4.10 the sample ($A=980.9\mu m^2$) has been irradiated applying $400W/cm^2$, 2mm/s, 78% overlapping and its specific resistance was measured **$\rho=14.7 \cdot \rho_{\text{bulk silver}}$** after the laser sintering process.
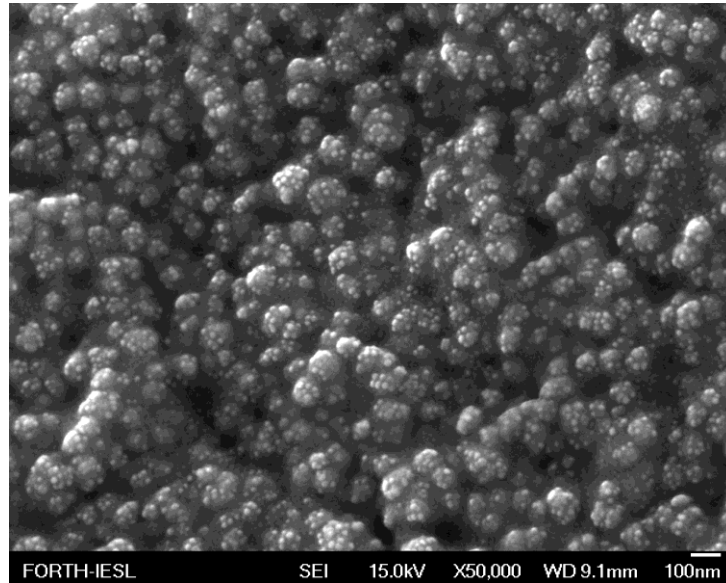
Figure 4.11: SEM image of Ag NPs structure with ρ=9.9•ρ $_{\text{bulk silver}}$.

In Figure 4.11 the sample (A=240.8μm^2) has been irradiated applying 400W/cm^2 , 2mm/s, 78% overlapping and the specific resistance was measured **ρ=9.9•ρ$_{\text{bulk silver}}$** after the laser sintering process.

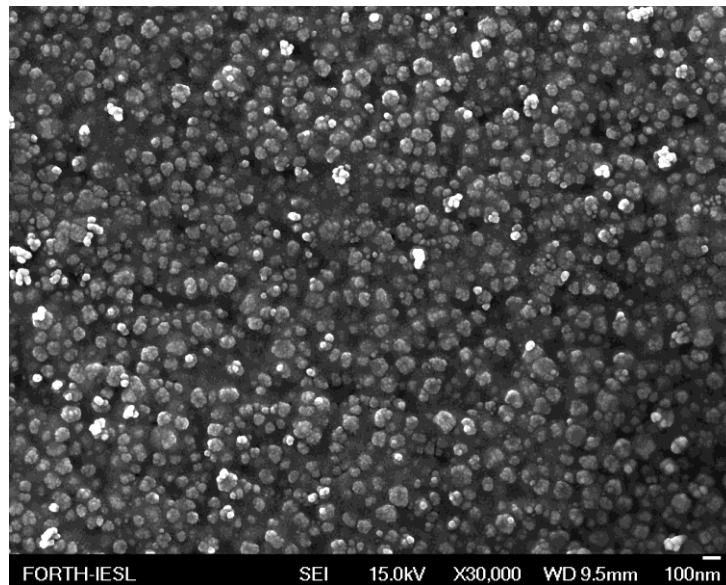**Figure 4.12**: SEM image of non-conductive Ag NPs structure.

In Figure 4.12 the sample (A=980.9μm^2) has been irradiated applying 750W/cm^2, 6mm/s, 78% overlapping and was found non-conductive after the laser sintering process.
SEM images of Figures 4.10 - 4.12 prove that an increase of the compactness has occurred after the laser irradiation also for the FR4 samples.

4.2.2 ZnO nanoparticle structures on glass.

The Experimental setup described in Section 3.3.1 was used to investigate the visible (**455**nm) CW laser sintering effect on printed semiconductor structures. As a first step of this investigation printed ZnO NPs structures described in Section 3.1 were irradiated using different values of Irradiance. Following the laser treatment samples were characterized using SEM images. In case of effective sintering of the structures the same system could be utilized in the development of semiconductor based sensors [20].
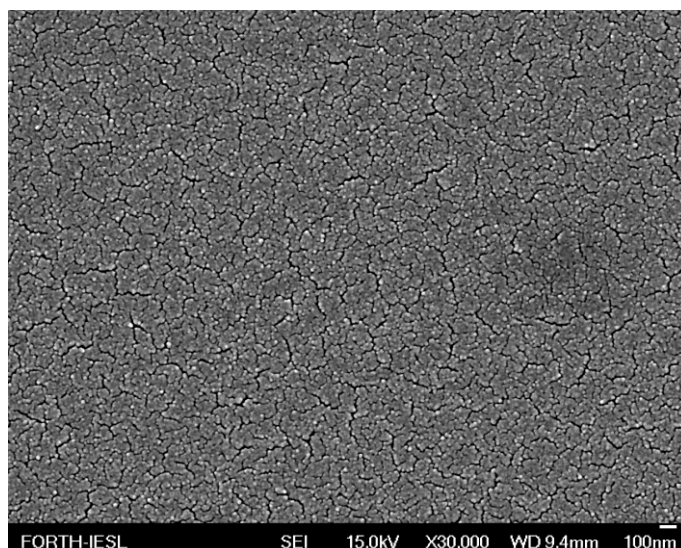

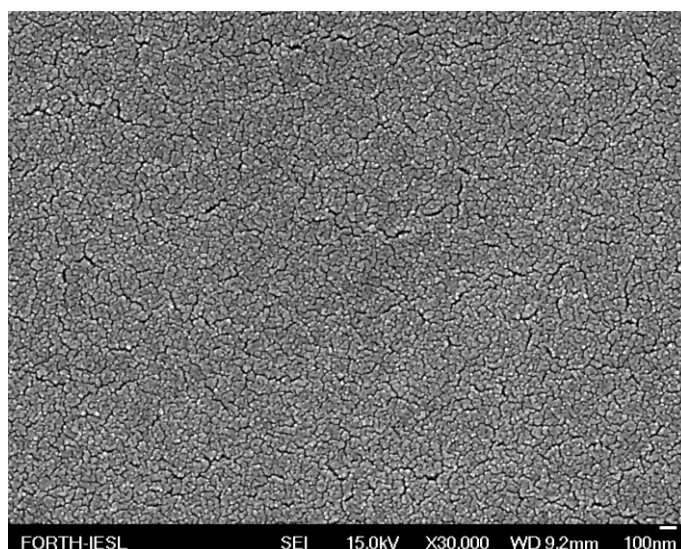**Figure 4.13**: SEM image of unirradiated ZnO NPs structure.

Figure 5.14: SEM image of laser sintered ZnO NPs structure, Irradiance 2640W/cm^2.
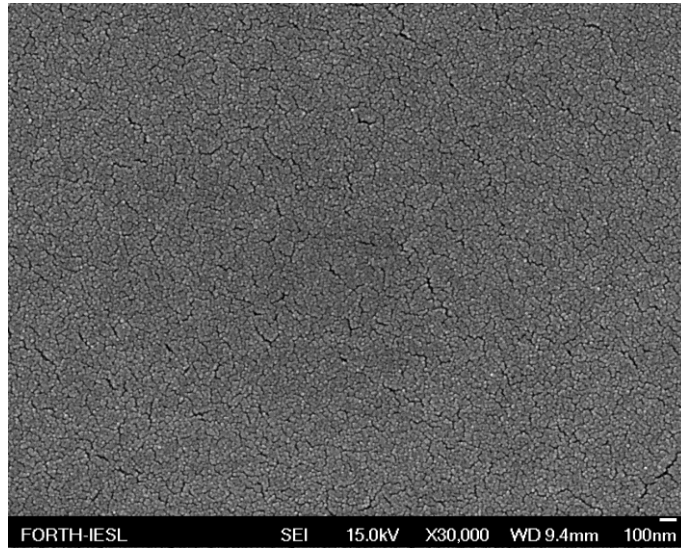
Figure 4.15: SEM image of laser sintered ZnO NPs structure, Irradiance: 560W/cm^2.

In Figure 4.14 – 4.15 the samples have been irradiated applying 78% overlapping with Scanning velocity 1.5 μm/s and two different values of Irradiance, 2640W/cm2 for sample in Figure 4.14 and 560W/cm2 for sample in Figure 4.15. A slight change of the compactness between the unirradiated structure and the sample irradiated with 2640W/cm2 can be observed in Figure 4.14. While in case of Figure 4.15 the difference with the unirradiated structure is clear as there is a significant decrease of the structure's pores and "cracks".

5. Discussion - Conclusions

In Table 10 the lowest measured specific resistance (ρ) values for each type (different cross section area) of sample are summarized ("K" is for kapton substrates).

#	Sample – cross section (μm^2)	Laser Sintering X $\rho_{bulk\ silver}$	Oven Sintering X $\rho_{bulk\ silver}$	Irradiance (W/cm^2)	Sc. speed (mm/sec)	Overlapping %	S. Resistance (μΩ*cm) PV nanocell A= 980.9 μm^2
1	325.3 (K)	8.7	5.7	400	2	Parallel	13.81
2	394.8 (K)	13	6.7	262	4	Parallel	20.63
3	427.3 (K)	12.8	5.1	400	2	15	20.39
4	521.8 (K)	8.8	4.5	500	8	78	14.08
5	619 (K)	13.5	5.4	500	4	45	21.52
6	1260.4 (K)	31.5	8.3	400	4	40	50.08
7	240.8	9.9	6.3	500	2	78	15.79
8	525.5	22.7	10.5	300	2	78	36.04
9	980.9	14.7	5.1	400	2	78	23.4

Table 10: Summary of the lowest measured ρ values.

Results of Table 10 prove that for relatively thin samples the sintering process was efficient as the minimum specific resistance values were close to the ones measured following oven sintering. Specifically, Ag lines on Kapton with A= 325.3μm^2 and FR4 with A=240.8μm^2 cross sections, exhibited ρ values smaller than the twice of oven sintering specific resistance. The sintering process applied for samples with larger dimensions was not efficient, resulting in ρ values above the double of that obtained upon oven sintering.
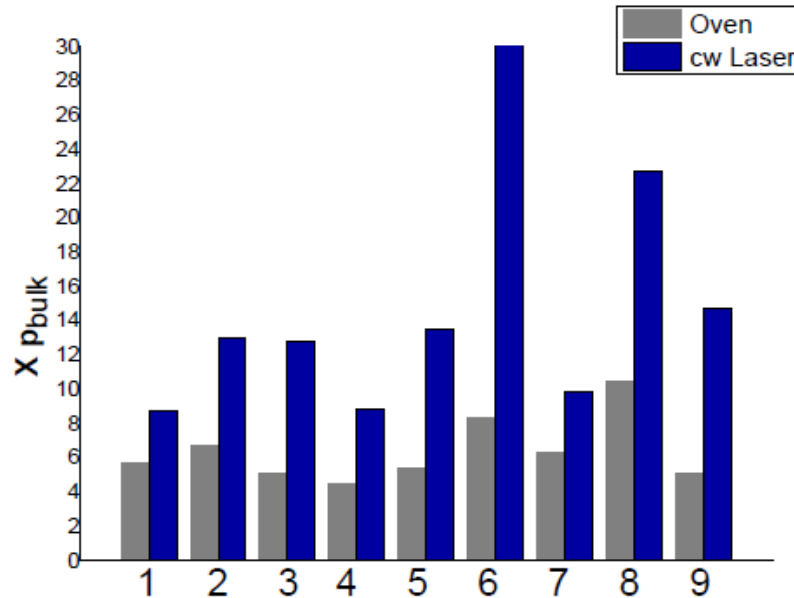
Graph 10: Comparison between CW laser and oven sintering.

According to the literature [21] CW laser achieve the partial melting of metal nanoparticles and local sintering is achieved. However it has been noticed that CW laser sintering does not enable the formation of uniformly sintered solid lines maybe due to the non-uniform spatial distribution of the beam. SEM images reveal that there is a remarkable modification of samples' surface for a suitable laser Irradiance value (Figures 4.5, 4.6, 4.10, 4.11). Formation of larger particles and a more compact surface are obtained. But these findings should be considered combined with electrical measurements, especially for larger samples. In case on ZnO pattern the reduction of the pores implies the presence of percolation "paths" throughout the material. We conclude that a nanostructured surface processed like this could be a potential candidate for gas applications [20], although further studies are required.

There is strong evidence that visible CW laser sintering set up developed during the present work is capable for producing high effective electrodes from printed metal NPs patterns and semiconducting nanostructures for potential applications. Further investigation over the experimental parameters and modification of the optical system could be the next steps for process improvement.

References

[1] P. Zhao, et al. , Journal of Mat. Process. Tech. 275 (2020) 116347

[2] Kravchuk O. and Reichenberger M. (2016) J Mater Sci Mater Electron 27(10):10934–10940

[3] A. M. Gaikwad et al, Appl. Phys. Lett. 102, 233302 (2013)

[4] W Gao et al., Acc. Chem. Res. (2019), 52, 523−533

[5] Kawahara J. et al (2013) J Polym Sci B Polym Phys 4:265–271

[6] William S. Wong and Alberto Salleo,"Flexible Electronics:Materials and Applications"ISBN,(2009) MIT

[7] O. Kravchuk et al. , "Sintering Methods of Inkjet-Printed Silver Nanoparticle Layers", Springer International Publishing AG (2018)

[8] Lesyuk R (2008) "Ink-jet formation of switching elements of chips using silver nanoparticles" New technologies, Vol. 2 (20). – P. 30

[9] Kravchuk O et al. (2014), Adv Mater Res 1038:49–55

[10] Kruth, J-P. et al., Rapid Prototyping Journal, Volume 11 (2005)

[11] Reinhold I, Hendriks CE, Eckardt R et al., J Mater Chem 19:3384–3388 (2009)

[12] Agrawal D. Advances in Powder Metallurgy, 361–379 (2013)

[13] P.V. Kazakevich et al. Applied Surface Science 252 (2006) 4373–4380

[14] F. Zacharatos et al., Materials (2018), 11(11), 2142

[15] P. Peng et al., Appl Phys A (2012) 108:685–691

[16] Navick, X.-F et al., Nuclear Instruments and Methods in Physics Research Section A. 520 (1–3): 189–192 (2004)

[17]https://en.wikipedia.org/wiki/FR4

[18] M. Zenou et al., J. Phys. D: Appl. Phys. 47 (2014) 025501 (11pp)

[19] A. Chiolerio et al. / Microelectronic Engineering 88 (2011) 2481–2483

[20] Bai Lin Zhu et al., J Mater Sci (2007) 42:5416–5420

[21] I. Theodorakos et al., Applied Surface Science (2014)

[22] Ch. Simitzi , Phd thesis, Uni. Of Crete (2014)